



α -Fe₂O₃ as a versatile and efficient oxygen atom transfer catalyst in combination with H₂O as the oxygen source

Yukun Zhao ^{1,2}, Chaoyuan Deng ^{1,2}, Daojian Tang¹, Liyong Ding ^{1,2}, Yuchao Zhang ^{1,2}, Hua Sheng¹, Hongwei Ji¹, Wenjing Song ^{1,2}, Wanhong Ma¹, Chuncheng Chen ^{1,2} and Jincai Zhao ^{1,2}

Haematite (α -Fe₂O₃) has been extensively investigated as a photoanode in photoelectrochemical water oxidation, but the product O₂ has a low economic value. Here we expand its applications to the production of value-added chemicals and report its ability to act as a versatile and efficient oxygen atom transfer catalyst under visible-light irradiation. A variety of organic compounds and inorganic anions were successfully oxidized to the corresponding monooxygenation products with high selectivity and Faradaic efficiency by using water as the sole oxygen source. Photoexcited holes generate iron-oxo species (Fe^{IV}=O) on α -Fe₂O₃ surfaces and the process of oxygen-atom transfer is proposed to proceed via a concerted two-hole transfer pathway that involves the transfer of oxygen atoms from the surface Fe^{IV}=O to the substrates. The present study proves α -Fe₂O₃ is an excellent all-inorganic heterogeneous catalyst to drive oxygen atom transfer reactions, and this strategy has significant potential for the synthesis of fine and high-value-added chemicals.

hotoelectrochemical (PEC) techniques have been extensively investigated for solar energy conversion (for example, water splitting)¹⁻³ and for environmental remediation via pollutant degradation⁴. The production of fine chemicals by a photocatalytic transformation of organic compounds within PEC systems has also been reported, and shows promising results. For example, a PEC system using BiVO4 as the photoanode was recently reported to realize the activation of the C-H bond of benzyl alcohol, cyclohexene and tetralin, which produced benzaldehyde, cyclohexanone and tetralone, respectively, using tert-butyl hydroperoxide as the oxygen source⁵. The oxidation of cyclohexane to produce cyclohexanol and cyclohexanone was also achieved on WO₃ photoanodes⁶. However, compared with the more traditional electrochemical⁷⁻⁹ and photochemical^{10,11} methods for organic transformations, synthetic PEC approaches remain underdeveloped at the current time. How to directly harvest photogenerated carriers (electrons or holes) to facilitate organic transformations at electrochemical interfaces remains to be explored.

Hematite $(\alpha - Fe_2O_3)$ has been considered one of the most promising photoanode materials in PEC studies, owing to its abundance, non-toxicity, stability and visible-light absorption^{12,13}. Previous studies on α -Fe₂O₃-based PEC reactions focused on light-driven water oxidation during water splitting for H₂ evolution. In water oxidation, the product O₂ possesses a low economic value. It is therefore desirable to explore alternative oxidation reactions that produce high-value-added chemicals in PEC systems^{5,14,15}. As reported very recently, the radical cations formed from the oxidation of electron-rich arenes by photoinduced holes on an α -Fe₂O₃ photoanode lead to an effective arene C–H amination with unusual *ortho* selectivity¹⁶. It has also been proved that, during water oxidation on α -Fe₂O₃ photoanodes, the holes trapped in the surface states—rather

than holes from the valence band—react with the adsorbed water and drive water oxidation¹⁷. These trapped holes have been identified as high-valent iron-oxo intermediates (Fe^{IV}=O) by operando attenuated total reflection-Fourier transform infrared spectroscopy¹², as well as soft X-ray (O 1s) spectroscopy¹⁸⁻²⁰. The high-valent iron-oxo characteristics of surface-trapped holes on α-Fe₂O₃ are reminiscent of such high-valent metal-oxo species, which are ubiquitous in biological systems and are extensively studied in catalytic oxygenation processes²¹⁻²³. For instance, oxygen atom transfer (OAT) reactions, which have been widely applied to produce important pharmaceutical intermediates (for example, sulfoxides and epoxides)^{24,25}, are commonly initiated by high-valent metal-oxo species. OAT involves a direct reaction between the oxygen atom of a high-valent metal-oxo centre and the lone-pair electrons of substrates, in which no free radicals are involved. Therefore, OAT reactions commonly have high chemo- or stereoselectivity²⁶. In metal-complex-based OAT systems, organic ligands are always used to modulate the microenvironments of metal centres²⁷. These organic ligands suffer damage under the strongly oxidizing OAT conditions, which makes these metal complexes rather unstable. In addition, the formation of high-valent metal-oxo species is usually achieved with the aid of extremely strong oxidizing peroxo species, such as H₂O₂, RCO₃H and PhIO (refs ²⁸⁻³⁰). Therefore, it is rather difficult to avoid undesirable by-products. Moreover, product separation is also problematic in these homogeneous systems. PEC approaches with metal oxide electrodes may address these shortcomings.

In this work, we report that α -Fe₂O₃ can serve as an effective heterogeneous OAT photocatalyst in PEC systems. Different transformations, which include sulfoxidation, C=C epoxidation, the oxygenation of Ph₃P and the monooxygenation of inorganic ions

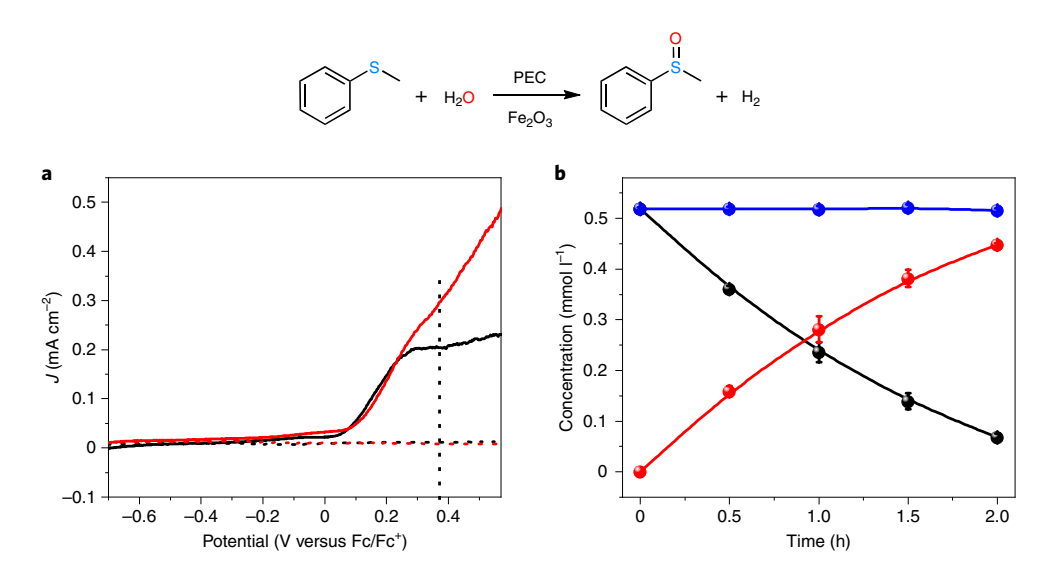


Fig. 1 | Linear sweep voltammetry and photoelectrolysis experiments of MPS oxidation. a, J-V scan of an α-Fe₂O₃ photoanode under AM 1.5G illumination (solid lines) and in the dark (dashed lines) measured in 0.1 M TBABF₄ (tetrabutylammonium tetrafluoroborate) solution (CH₃CN with 5% H₂O, 20 ml) under an Ar atmosphere without (black) and with (red) 10.0 mM MPS. The dashed vertical line indicates the potential (0.37 V versus Fc/Fc⁺) at which the photoelectrolysis experiments were conducted. **b**, The decay of MPS (black line), the evolution of MPSO (red line) and the total sulfur balance (the sum of the remaining MPS and the generated MPSO (the blue line)) during the PEC oxidation of MPS (0.5 mM). The error bars are the s.d. of three parallel repeated results.

(nitrite and arsenite), were achieved with a high selectivity and Faradaic efficiency (FE). In contrast, on the most commonly used photocatalyst, TiO₂, much lower efficiencies were observed under identical PEC conditions. H₂ ¹⁸O-isotope labelling experiments and detailed product analysis demonstrated that water is the only oxygen atom source for these OAT reactions. Rate-law analysis on the surface-trapped holes exhibited a two-hole transfer process, which supports the transfer of oxygen atoms from the surface iron-oxo species to substrates in these reactions.

Results

PEC oxygenation reactions on α -Fe₂O₃. α -Fe₂O₃ photoanodes were fabricated on fluorine-doped tin oxide (FTO) glass substrates in accordance with the literature³¹ and were characterized by scanning electron microscopy, X-ray diffraction spectroscopy and X-ray photoelectron spectroscopy (see Supplementary Fig. 1 for details). The configuration of PEC cells used in this work is shown in Supplementary Fig. 2. The PEC OAT reaction on α-Fe₂O₃ was first examined by the oxygenation of sulfide, which is widely used to investigate OAT reactions³² and can produce sulfoxide products with important applications in pharmaceuticals and agrochemicals^{24,33}. Linear sweep voltammetry showed that, under AM 1.5G irradiation, the onset potential was approximately 0.05 V versus Fc/Fc⁺ in a solution of CH₃CN with a small amount of water (5%) (Fig. 1a). In the presence of methyl phenyl sulfide (MPS), the onset potential and the initial photocurrent did not change much. However, when the bias was above 0.25 V versus Fc/Fc+, the photocurrent with MPS began to exceed that without MPS. In addition, the difference became enlarged with an increasing applied bias, which suggests the participation of MPS in the oxidation reaction on α -Fe₂O₃ surfaces. In the dark, a very low current was detected, which indicates that the direct electrochemical oxidation of MPS is negligible under the present conditions.

To investigate the products of MPS oxidation, photoelectrolysis experiments were conducted at 0.37 V versus Fc/Fc⁺ in an Ar atmosphere. Product analysis by high-performance liquid chromatography (HPLC) showed that MPS was converted into methyl phenyl sulfoxide (MPSO) in a nearly quantitative manner during

the whole PEC process, which lasted two hours, wherein approximately $86.6 \pm 1.6\%$ of MPS was oxidized (Fig. 1b). The FE for the formation of MPSO was $92.1 \pm 5.8\%$, which accompanied H₂ production at the cathode with a FE of 95.0% (Supplementary Fig. 3). The FE increased $(93.8 \pm 2.0\%)$ with higher MPS concentrations (Table 1, entry 4, and Supplementary Fig. 4). A high selectivity and FE of MPSO formation were also observed with varied water contents (from 5 to 20%) (Table 1, entries 1–3, and Supplementary Fig. 5). The high FE indicates that the oxidation of MPS preferentially occurs, and water oxidation is largely depressed by the competition between MPS and water molecules for the photogenerated holes. The recycling experiments showed that the PEC performance for MPS oxidation of the α-Fe₂O₃ photoanode remained unchanged after five repeated experiments (Supplementary Fig. 6). Moreover, X-ray diffraction spectra indicated that the structure of the α-Fe₂O₃ film was not changed after a PEC reaction of five cycles (Supplementary Fig. 7), which confirms the stability of the α -Fe₂O₃ photoanode in the PEC process. The monochromatic incident photon-to-electron conversion efficiency measurement showed that the visible-light activity started at ~550 nm and increased with the shortened wavelength. This efficiency exhibited a maximum value at a wavelength of 330 nm, and increased with increasing concentrations of MPS, which reached ~22% using 10.0 mM of MPS (Supplementary Fig. 8).

The high selectivity on α -Fe₂O₃ is in sharp contrast with the unselective degradation of organic compounds on other metal oxide photocatalysts (for example, TiO₂) in the presence of water. It is well-known that TiO₂ is very effective for the oxidation of H₂O/OH⁻ to hydroxyl radical, which leads to the unselective degradation of organic substrates^{34,35}. To highlight the highly selective characteristic of α -Fe₂O₃ towards PEC oxidation reactions, PEC oxidation of MPS was further examined on TiO₂ as a comparison. The TiO₂ photoanode was prepared by a hydrothermal method and characterized by scanning electron microscopy, X-ray diffraction spectroscopy and X-ray photoelectron spectroscopy (see Supplementary Fig. 9 for details). For comparison, two applied biases were conducted on the TiO₂ photoanode: 0.37 V versus Fc/Fc⁺ (which was the same as that on α -Fe₂O₃) and -0.13 V versus Fc/Fc⁺ (which produced a

NATURE CATALYSIS ARTICLES

Table 1 | Conversion, selectivity and FE for PEC oxygenation reactions of various substrates on α -Fe₂O₃ and TiO₂^a

February Substrates Photography Solvent (9/ No. 2004) Solvent (9/ No. 2

, , , , , , , , , , , , , , , , , , , ,						
Entry	Substrate	Photoanode	Solvent (% H ₂ O)	Conversion (%) ^b	Selectivity (%) ^c	FE (%) ^d
1	MPS	α -Fe ₂ O ₃	CH ₃ CN (5)	86.6 ± 1.6	99.3 ± 0.7	92.1 ± 5.8
2	MPS	α -Fe $_2$ O $_3$	CH ₃ CN (10)	94.3 ± 2.5	99.4 ± 0.2	87.6 ± 2.2
3	MPS	α -Fe ₂ O ₃	CH ₃ CN (20)	95.5 ± 4.5	99.4 ± 0.1	85.5 ± 1.5
4e	MPS	α -Fe ₂ O ₃	CH₃CN (5)	66.7 ± 6.5	95.2 ± 2.0	93.8 ± 2.0
5	MPS	TiO ₂	CH₃CN (5)	9.3	84.0	2.3
6 ^f	MPS	TiO ₂	CH₃CN (5)	13.6	88.9	13.8
7	p-NO ₂ -MPS	α -Fe $_2$ O $_3$	CH₃CN (5)	53.7 ± 15.0	92.1±6.5	76.3 ± 8.5
8	p-F-MPS	α -Fe $_2$ O $_3$	CH₃CN (5)	79.6 ± 9.1	97.7 ± 1.5	85.8 ± 4.1
9 ^g	p-CH₃-MPS	α -Fe ₂ O ₃	CH₃CN (5)	84.4 ± 6.3	98.1 ± 1.4	95.9 ± 1.1
10 ^h	p-OCH ₃ -MPS	α -Fe $_2$ O $_3$	CH₃CN (5)	77.7 ± 6.7	98.0 ± 1.6	93.2 ± 2.4
11	Cyclohexene	α -Fe ₂ O ₃	CH₃CN (5)	79.9 ± 5.4	62.1 ± 3.6	45.5 ± 1.6
12 ⁱ	Cyclooctene	α -Fe $_2$ O $_3$	CH₃CN (5)	82.2 ± 9.1	8.7 ± 0.5	2.7 ± 0.2
13 ^j	trans-stilbene	α -Fe $_2$ O $_3$	CH₃CN (5)	82.1 ± 0.9	72.1 ± 2.0	11.6 ± 0.8
14	Ph₃P	α -Fe ₂ O ₃	CH₃CN (5)	92.5 ± 6.4	99.6 ± 0.3	98.5 ± 0.8
15	Nitrite	α -Fe $_2$ O $_3$	H ₂ O	91.5 ± 3.3	93.2 ± 1.9	86.7 ± 1.3
16	Nitrite	TiO ₂	H ₂ O	32.0	93.8	14.9
17	Arsenite	α -Fe $_2$ O $_3$	H ₂ O	90.0 ± 5.0	98.5 ± 1.1	92.0 ± 2.5
18	Phosphite	α -Fe $_2$ O $_3$	H ₂ O	0.5	-	-
19	Phosphite	TiO ₂	H ₂ O	37.3	96.0	61.5
20	MPS no light	α -Fe $_2$ O $_3$	CH₃CN (5)	0	-	-
21	MPS no bias	α -Fe $_2$ O $_3$	CH₃CN (5)	0	-	-

a The corresponding concentrations of the substrates, the concentrations of the monooxygenation products and the total charge in the process of photoelectrolysis are listed in Supplementary Table 1.
Conversion rate for a PEC reaction. Typical reaction conditions unless otherwise stated: in CH₃CN systems, 0.1M TBABF₃, was used as the electrolyte and the initial concentration of the substrates was 0.2 mM. PEC reactions were carried out for 2 h under AM 1.5G illumination at 0.37 V versus Fc/Fc⁺ in a CH₃CN system (20 ml) and at 1.42 V versus reversible hydrogen electrode in the aqueous system (100 ml). All the error bars are defined in the legends (s.d.) together with a measure of the mean. Selectivity of monooxygenation products. ⁴EE estimated from the charge consumption of monooxygenation products and the total charge through the circuit.
At an MPS concentration of 10.0 mM (10 ml) and an applied potential of 0.57 V versus Fc/Fc⁺ for 5 h of electrolysis. PEC oxidation at −0.13 V versus Fc/Fc⁺. ♣After photoelectrolysis for 1.5 h. After photoelectrolysis for 1 h. The initial concentration of cyclooctene was 0.2 mM, and photoelectrolysis was conducted at 0.57 V versus Fc/Fc⁺ for 1 h. To avoid the direct excitation of *trans*-stilbene, a 420 nm long-pass filter was used.

comparable photocurrent to that with $\alpha\text{-Fe}_2O_3$). At both biases, a relatively low selectivity was observed (Table 1, entries 5 and 6). Moreover, the conversion of MPS was much lower than that on $\alpha\text{-Fe}_2O_3$, although the photocurrent was higher than that on $\alpha\text{-Fe}_2O_3$ (Supplementary Fig. 10). Accordingly, very poor FE values (2.3% at 0.37 V versus Fc/Fc+ and 13.8% at -0.13 V versus Fc/Fc+) were obtained (Table 1, entries 5 and 6, and Supplementary Fig. 11). In addition, the partial current density for MPSO generation on TiO₂ was estimated to be only ~ 0.01 mA cm⁻² at 0.37 V versus Fc/Fc+, much lower than that on $\alpha\text{-Fe}_2O_3$ (~ 0.1 mA cm⁻²). Moreover, the photocurrent on TiO₂ underwent a rapid decay due to the formation of many by-products on the photoanode surface to block active sites (Supplementary Figs. 12 and 13). All these results suggest that the oxidation of MPS on TiO₂ is quite ineffective and unselective, and is much less competitive than water oxidation under the present conditions.

PEC sulfoxidation reactions of a series of *para*-substituted MPS substrates were further tested. High selectivity and FE were obtained for all the monosubstituted MPS derivatives (Table 1, entries 7–10). Specifically, MPS derivatives with electron-donating groups (for example, –OCH₃, –CH₃) were oxidized at rapid reaction rates (Supplementary Fig. 14) and transformed into their mono-oxygenated products. Moreover, the FE values were also higher than that of the unsubstituted MPS. However, the reaction rate, selectivity and FE were somewhat decreased by substitution with electron-withdrawing groups (for example, –NO₂). The Hammett linear free-energy relationship showed a negative slope of –0.43

(Supplementary Fig. 15), which indicates a positively charged transition state on MPS in the rate-determining step^{36,37}.

The PEC oxidation of cyclohexene and cyclooctene, which are frequently investigated as models of homogeneous OAT reactions^{27,38}, was also explored on α-Fe₂O₃ (Supplementary Figs. 16 and 17). The cyclohexene was oxidized to cyclohexene oxide with a selectivity of $62.1 \pm 3.6\%$, and the corresponding FE value was $45.5 \pm 1.6\%$ (Table 1, entry 11). The selective production of epoxide in the cyclohexene oxidation on α -Fe₂O₃ is quite different from the PEC oxidation of cyclohexene on BiVO₄, where the formation of cyclohexanone was reported to be dominant⁵. In the oxidation of cyclohexene on BiVO₄, the formation of a carbon-centred radical by C-H activation is involved, and the formed radical receives an oxygen atom from tert-butyl hydroperoxide to produce cyclohexanone⁵. Such a difference in products suggests that the oxidation of olefin substrates on α-Fe₂O₃ should not occur via the C-H activation process by a radical pathway, as in the case of BiVO₄. However, for the epoxidation of cyclooctene, the selectivity to produce cyclooctene oxide was quite low $(8.7 \pm 0.5\%, \text{ Table 1}, \text{ entry 12},$ and Supplementary Fig. 17). Such an inefficiency probably stems from the large steric hindrance of the cyclooctene molecule, which inhibits the direct interaction of the α -Fe₂O₃ surface with the C=C bond. Apart from these aliphatic alkenes, a typical aromatic alkene (trans-stilbene) was also tested for the OAT reaction on α-Fe₂O₃ (Supplementary Fig. 18). It was found that the trans-stilbene was transformed to trans-stilbene oxide with a quite high selectivity $(72.1 \pm 2.0\%, \text{ Table 1}, \text{ entry 13})$, which supports the occurrence of

Fig. 2 | pK_a values and structural diagrams. Structural diagrams of nitrite, arsenite and phosphite under pH 7.0. The nitrite and arsenite possess unpaired electrons that are able to accept the oxygen atom from the O-atom donor, whereas phosphite cannot.

OAT pathway during the oxidation of alkene on the α -Fe₂O₃ photo-anode. For the PEC oxidation of Ph₃P (Supplementary Fig. 19), another well-studied OAT substrate in metal-complex-based systems^{28,39}, an excellent selectivity (99.6 \pm 0.3%) and FE (98.5 \pm 0.8%) for the monooxygenation product (Ph₃PO) formation were also obtained on α -Fe₂O₃ (Table 1, entry 14).

OAT reactions are also frequently studied in inorganic chemistry. For example, the oxidation of nitrite (NO₂⁻) by a number of oxygen atom donors, such as the trans-dioxoruthenium(VI) complex, was reported to occur via an OAT pathway⁴⁰. Arsenite also tends to directly accept an oxygen atom from peroxymonosulfate⁴¹. In the present study, we examined PEC oxidation of low-valent oxyacids of the main group V non-metal elements, to which the nitrogen and arsenic belong, in 0.1 M Na₂SO₄ aqueous solution. As shown in Supplementary Fig. 20, a significant increase in the photocurrent density was observed with the addition of nitrite and arsenite, which demonstrates that these two ions were efficiently oxidized on α-Fe₂O₃. Product analysis showed that nitrite and arsenite were oxidized to nitrate and arsenate with FEs of $86.7 \pm 1.3\%$ and $92.0 \pm 2.5\%$, respectively (Table 1, entries 15 and 17). Surprisingly, the addition of phosphite did not influence the photocurrent, and little oxygenation product (that is, phosphate) was detected (Supplementary Fig. 20c,f). By contrast, on TiO, photoanodes (Table 1, entries 16 and 19), the FE of nitrite oxidation was quite low (14.9%), whereas the phosphite oxidation was quite efficient (FE = 61.5%).

At pH 7.0, nitrite is in the form of NO₂⁻ (p K_a = 3.4, equation (1)). For phosphite, the dominant state should be HPO₃²⁻ (the p K_a of hydrogen phosphite is 6.7, equation (2)), whereas arsenite remains in its neutral form (As(OH)₃, p K_a = 9.2, equation (3)):

$$HNO_2 \leftrightarrow H^+ + NO_2^- \quad pK_a = 3.4 \tag{1}$$

$$HP(O)_{2}(OH)^{-} \leftrightarrow HPO_{3}^{2-} + H^{+} pK_{a} = 6.7$$
 (2)

$$As(OH)_3 + H_2O^- \leftrightarrow As(OH)_4^- + H^+ \quad pK_a = 9.2$$
 (3)

As shown in Fig. 2, the nitrite and arsenite ions possess lone pair σ orbitals to accept the oxygen atom from the O-atom donor. However, for phosphite, the hydrogen atom bonded directly to the phosphorus atom is not readily ionizable. Accordingly, no orbital with lone-pair electrons is available for the electrophilic attack of the O-atom donor. The direct one-electron oxidation or hydrogen abstraction from the P–H bond by OH radicals should be more favourable than the OAT reaction, which should be responsible for the efficient oxidation of phosphite on TiO₂.

Identification of oxygen atom source. $H_2^{18}O$ isotopic labelling experiments were performed to further investigate the oxygen atom source in the PEC oxidation of MPS. As shown in Fig. 3b, the prominent molecular ion peak of MPSO appeared at a mass-to-charge ratio (m/z) of 140.1 when $H_2^{16}O$ was used in an Ar atmosphere. After replacement of $H_2^{16}O$ with $H_2^{18}O$ in an Ar atmosphere (Fig. 3a), this peak shifted to 142.1, and the relative abundance of m/z = 140.1 was quite small (6.1%). The ion peak of the demethylation fragment

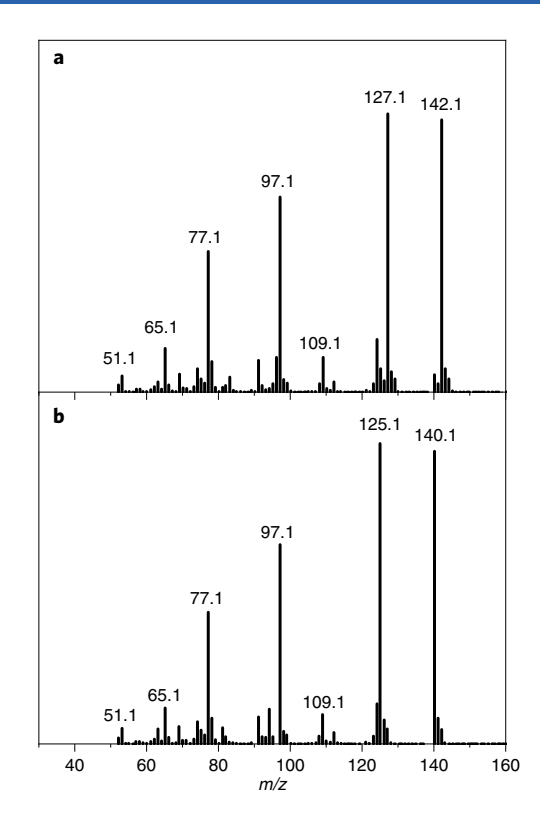


Fig. 3 | Mass spectra of MPSO. a,b, Mass spectra of MPSO generated during the oxidation of MPS on α -Fe₂O₃ in the presence of H₂¹⁸O (**a**) and H₂¹⁶O (**b**).

 $(C_{\epsilon}H_{\epsilon}SO \text{ fragment}, m/z=125.1)$ also shifted from 125.1 to 127.1. These results indicate that water acts as the only oxygen atom source for the oxidation of MPS to MPSO on α-Fe₂O₃. In the presence of ¹⁶O₂, when H₂¹⁸O was used, the prominent molecular ion peak of MPSO was at m/z 142.1 (Supplementary Fig. 21). Moreover, the ion peak of the demethylation fragment (C₆H₅SO fragment, m/z=125.1) also shifted to 127.1, which is similar to the isotope shift under anaerobic conditions. This result shows that, even in the presence of O₂, the oxygen source in the formed MPSO is still from H₂¹⁸O, and the O₂ cannot incorporate its oxygen atom into the produced MPSO. In addition, for the epoxidation of cyclooctene on α-Fe₂O₃, the molecular ion peaks for the formed cyclooctene epoxide shifted from m/z 126.1 to 128.1 in the presence of H₂¹⁸O. The peaks of fragments that contained the O atoms (for example, m/z = 111.1, 97.1 and 83.1) also shifted by two m/zunits (Supplementary Fig. 22), which confirms that water serves as the oxygen atom source in the cyclooctene epoxidation reaction, in spite of its low selectivity.

In previous photochemical organic transformation studies, photocatalytic oxidation of organic sulfides with a selectivity of >98% was also reported with Pt/BiVO₄ photocatalysts¹¹. Moreover, the isotope study with H₂¹⁸O also demonstrated that water was the oxygen source for the formed sulfoxide products. In this case, a noble metal (Pt) was used to separate electron–hole pairs and prevent electron-induced reactive oxyradicals (O₂•-, •OOH and so on). In our PEC system, both the charge separation and the inhibition of electron-induced reactive oxyradicals are achieved well by the separated photoanodes and cathodes, and thus the noble metal co-catalysts are no longer needed.

Surface hole-trapping states. Earlier work has shown that water oxidation on $\alpha\text{-Fe}_2O_3$ proceeds via surface-trapped holes rather than via direct hole transfer from the valence band at low anodic

NATURE CATALYSIS ARTICLES

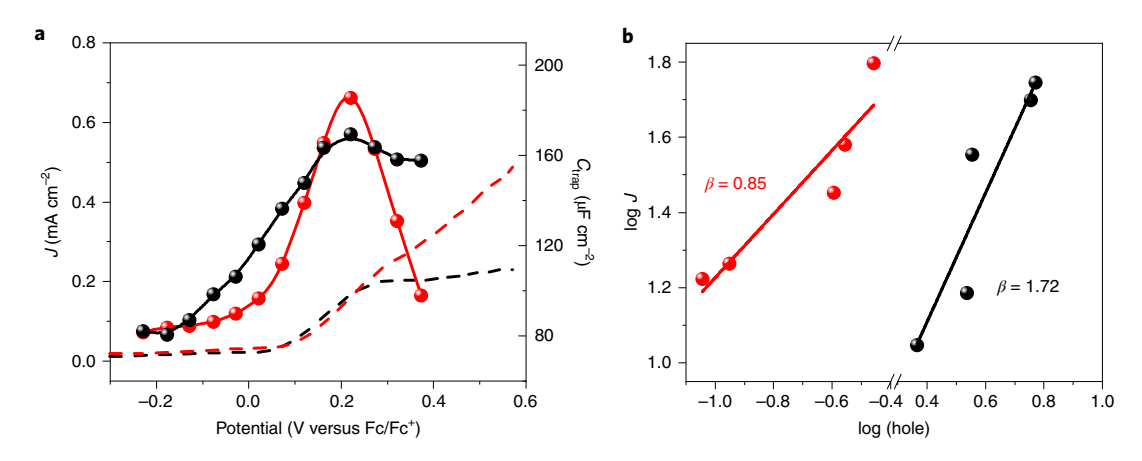


Fig. 4 | Surface-hole trapping states based on EIS data. a, J-V curves (dashed lines) and C_{trap} values (solid lines and dots) obtained on α-Fe₂O₃ with MPS (red) and without MPS (black) under AM 1.5G illumination. **b**, Relationship between the photocurrent density (μ A cm⁻²) and surface-hole density (number of holes nm⁻²) for α-Fe₂O₃ (black) and TiO₂ (red) photoanodes in 10.0 mM MPS solution.

potentials ^{17,42}. To reveal the role of these surface holes in oxygenation reactions, electrochemical impedance spectroscopy (EIS) was used to investigate the reaction kinetics of MPS oxidation on $\alpha\text{-Fe}_2O_3$ (Supplementary Fig. 23). Figure 4a showed the variations in the fitted capacitance of surface states (C_{trap}) with applied potentials. Regardless of the presence of MPS, C_{trap} increased with the applied bias at low potentials and reached its maximum at approximately 0.25 V versus Fc/Fc+ due to the accumulation of surface holes. After that, C_{trap} began to decrease due to the increased consumption rate of surface-trapped holes. These results indicate that, similar to water oxidation, the oxygenation of MPS on $\alpha\text{-Fe}_2O_3$ is also mediated by surface-trapped holes. Furthermore, the decrease of C_{trap} in the presence of MPS was faster than that in the pure electrolyte, confirming that the consumption of surface-trapped holes by MPS oxygenation is faster than that by water oxidation.

Further rate law analysis based on EIS measurements under varied light intensities (Supplementary Fig. 24 and Supplementary Tables 4 and 5) showed that the reaction order of surface-trapped holes during MPS oxidation was approximately 1.72 on α -Fe₂O₃ but about 0.85 on TiO₂ (Fig. 4b), indicating that MPS oxygenation reactions on α -Fe₂O₃ and TiO₂ tend to be second-order and first-order reactions with respect to surface-trapped holes, respectively. As depicted in Supplementary Figs. 25, 26 and Supplementary Tables 6 and 7, similar differences in the reaction orders were observed for the oxidation of nitrite (β =1.82 and β =0.95 on α -Fe₂O₃ and TiO₂, respectively). The second-order reaction kinetics indicate that two-hole transfer is involved in the rate-limiting step of OAT reactions on α -Fe₂O₃. In contrast, the reaction on TiO₂ was dominated by transfer of a single surface-trapped hole, which is consistent with the well-known free radical characteristics of TiO₂.

The proposed mechanism. It is believed that surface-trapped holes are formed from hole transfers to surface-coordinated hydroxyl groups with a concomitant deprotonation step (step (1) in Fig. 5)^{13,43,44}. According to the analysis of the density of states (DOS) using spin-polarized density functional theory (DFT)+U (full details of the DFT calculations are given in Methods), these surface states are located in the mid gap of α -Fe₂O₃ and consist of the hybridized O 2p and Fe 3d orbitals (Supplementary Fig. 27a). Chemically, the trapping of holes on these hybrid surface states could lead to the formation of high-valent iron–oxo (Fe^{IV}=O) species⁴⁵. The chemical nature of these iron–oxo species should be analogous to that of the iron–oxo centres of biologically inspired haem and non-haem complexes³⁰. One of the most famous reactions of these Fe^{IV}=O-based complexes is OAT, in which the oxygen in Fe^{IV}=O is transferred to

the substrate orbital with lone-pair electrons^{29,32}. In contrast to the single-site Fe^{IV}=O in complex molecules, the semiconductor characteristics of α-Fe₂O₃ enable the accumulation of surface Fe^{IV}=O sites and the facile hopping of these sites on surfaces. As shown in Fig. 4a, the accumulation of surface-trapped holes suggests that this process requires a sufficient Fe^{IV}=O density. During the accumulation of surface holes, it is also possible that two electrons are removed from one Fe-O site to form a Fe^V=O species, which has also been reported to be active for driving OAT reactions^{46,47}. However, our theoretical calculations showed that the energy increase for the Fe^V=O formation was higher than that of the adjacent two Fe^{IV}=O sites (Supplementary Fig. 28), which indicates that the formation of Fe^V=O is thermodynamically unfavourable relative to the formation of the adjacent two Fe^{IV}=O sites. Therefore, we conclude that the adjacent two Fe^{IV}=O sites should be the active sites for the OAT reactions under the present experimental conditions.

Before the OAT step occurs, it is plausible that the nucleophilic attack of a substrate on the oxygen atom of the Fe^{IV}-oxo results in the formation of an intermediate complex (step (2) in Fig. 5), which would attract other surface-hole hopping to neighbouring sites. Given the second-order characteristics of the hole kinetics, it is speculated that the following OAT step is the rate-limiting step and should be concerted with the electron transfer from the adjacent Fe^{IV}-oxo site on α -Fe₂O₃ surfaces (as shown in step (3) in Fig. 5). This rate-limiting step involves cleavage of a Fe-O bond, formation of an X-O bond and a concerted hole transfer from the adjacent trapped hole. Accordingly, two holes, together with the oxygen dianion, are transferred in a concerted manner from α-Fe₂O₃ to the substrates. After this transition state, the departure of the oxygen atom and the release of the oxygenated product (XO) result in unoccupied surface FeIII sites. The adsorption and dissociation of water at these sites regenerate the surface hydroxyl groups to terminate the catalytic cycle (step (4) in Fig. 5). In step (4), the oxygen atom in water participates in the catalytic process and is finally incorporated into oxygenation products. During the OAT reaction via the single-site Fe^{IV}=O complexes, the oxygenation of the substrate would lead to the formation of Fe^{II} (ref. 48). It is also possible that the OAT reaction on α-Fe₂O₃ is determined by a similar step to that on the single-site $Fe^{IV} = O$ complexes ($Fe^{IV} = O + X \rightarrow Fe^{II} + OX$). In this step, only one Fe^{IV}=O site is involved, which should correspond to the first-order kinetics with respect to surface-trapped holes. However, our experimental results show that the OAT reaction on α-Fe₂O₃ follows second-order kinetics, which suggests that a two-hole transfer is involved in the rate-limiting step. Therefore, we exclude the possibility that the only one Fe^{IV}=O site is involved

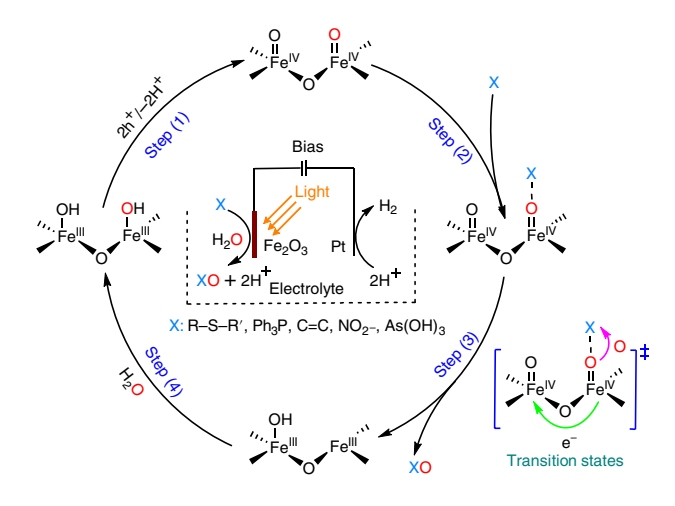


Fig. 5 | PEC OAT reactions with H₂O as an oxygen atom source on α-Fe₂O₃. The scheme indicates the generation of iron-oxo species (Fe^{IV}=O) on α-Fe₂O₃ surfaces via photoexcited holes (step (1)). Step (3) describes the transfer of oxygen atoms from the surface Fe^{IV}=O to the substrates with a concerted two-hole transfer pathway. Finally, water molecules replenish the consumed oxygen atoms in the catalytic cycle by adsorption and dissociation (step (4)).

in the rate-limiting step. It is reported that a three-hole transfer is involved in the rate-determining step of water oxidation on $\alpha\text{-Fe}_2O_3$ (refs 13,43,44). In this process, after the two-hole oxidation of two surface Fe sites to form two nearest-neighbour Fe IV =O species, the third hole oxidizes one of the Fe IV =O groups to Fe V =O, which gains enough oxidation power to drive water oxidation 42 . In the present study, we showed that the presence of substrates can deplete the two nearest-neighbour Fe IV =O species by OAT to the substrates. As a result, the substrate is oxygenated and water oxidation is suppressed.

The different PEC behaviours in the OAT reactions between α-Fe₂O₃ and TiO₂ should originate from their distinct electronic structures. As shown in the DOS results (Supplementary Fig. 27), the states of trapped holes on TiO₂ surfaces consist of O 2p orbitals¹⁹. Therefore, surface-trapped holes on TiO₂ behave similarly to that of a highly active oxygen-centred radical (O•-). However, although both Fe 3d and O 2p orbitals contribute to the surface state of α -Fe₂O₃, the Fe 3d orbitals are energetically lower than the O 2p orbitals. As a result, the surface hole is trapped in the Fe 3d orbitals to form Fe^{IV}=O species rather than in the O 2p orbitals to generate O^{•-} radicals. Our DFT calculations showed that the DOS of H₂O adsorbed at the surface states on α-Fe₂O₃ was distributed well below the DOS of the surface states (Supplementary Fig. 27a), which suggests that a single-hole transfer from the surface states of α -Fe₂O₃ to the adsorbed H₂O is thermodynamically unfavourable. This result is in agreement with the earlier report that three holes are required for surface to gain enough oxidation power to drive water oxidation^{13,43,44}. By contrast, on TiO2, the DOS from the adsorbed H2O located above those of surface states (Supplementary Fig. 27c), which implies that the photoinduced hole in TiO₂ is able to transfer to the adsorbed H₂O.

Conclusions

We have developed a PEC strategy to conduct OAT reactions on $\alpha\text{-Fe}_2O_3$ under mild conditions. A wide variety of substrates, which included thioethers, olefins, Ph_3P and inorganic salts, can be oxygenated by using water as the only oxygen atom source. The excellent oxygenation selectivity and FE can both exceed 90.0% for most substrates. Based on EIS and DFT studies, surface-trapped holes are verified to play a pivotal role in the OAT mechanism. We believe that this PEC strategy has significant potential for various oxygenation reactions of fine and value-added chemicals.

Methods

Photoanode preparation. α-Fe₂O₃ photoanodes were prepared by a two-step method according to the literature³¹. Initially, anhydrous iron(III) chloride (2.43 g) and sodium nitrate (0.85 g) were added to 100 ml of deionized water with 5 min of stirring, and then the obtained solution was transferred into the reaction kettle with a piece of clean FTO glass (ultrasonic in acetone, ethanol and water for 30 min, sequentially). Then, iron oxyhydroxides (FeOOH) were grown on the FTO glass through a hydrothermal method at 95 °C for 4h. The obtained FeOOH was sintered at 550 °C for 2 h in a temperature-programmed process and subsequently annealed at 750 °C for 15 min. For the synthesis of TiO₂ (rutile) photoanodes, titanium *n*-butoxide (0.8 ml) was added into a hydrochloric acid solution (30 ml of 35–37% HCl and 30 ml of deionized water), which needed to be stirred for 30 min. Then, the above solutions and FTO glass were transferred to a Teflon reactor to synthesize the precursor by a hydrothermal method (150 °C for 4 h). The obtained precursor was washed with deionized water and annealed at 450 °C for 1 h.

Electrochemical study. Electrochemical experiments were conducted with a single-chamber electrochemical cell in an Ar atmosphere (Ar flow rate of 20 ml min-1). Platinum and the photoanodes were used as the counter and working electrodes, respectively. An Ag/AgCl electrode (3.5 M KCl leak-free and 2.0 mm diameter, Innovative Instruments) was used as the reference electrode. The PEC experiments were conducted by using a Metrohm Autolab electrochemical workstation, A 500 W Xe lamp (AULIGHT) with an AM 1.5G filter was used to serve as the reaction light source and the light intensity was adjusted to 100 mW cm⁻², as measured by an optical power meter (CEL-NP2000-10). A scan rate of 0.05 V s⁻¹ was used for linear sweep voltammetry experiments. For EIS measurements, a sinusoidal voltage pulse of 10 mV amplitude was applied on a bias potential, with frequencies that ranged from 100 kHz to 0.1 Hz. For the oxidation of inorganic ions (nitrite, arsenite and phosphite), the PEC experiments were carried out in an aqueous solution (pH = 7.0) with 0.1 M Na, SO₄ as the electrolyte. The PEC oxidation of organic substrates (thioether, olefins and Ph₃P) were conducted in CH₃CN with different amounts of H₂O, using 0.1 M TBABF₄ as the electrolyte. As shown in Supplementary Fig. 29, the potentials (versus Ag/AgCl) were calibrated using a 5.0 mM ferrocene/ferrocenium redox couple (E(versus Fc/ Fc^+) = E(versus Ag/AgCl) - 0.43 V.

Product analysis. MPS, MPSO, Ph₃P and Ph₃PO, *trans*-stilbene and *trans*-stilbene oxide were analysed and quantified by using an Agilent HPLC1260 system with a Dikma Diamond C-18(2) column (250 \times 4.6 mm, 5 μm film thickness). For the detection of MPS and MPSO, acetonitrile (65%) and water (35%) were used as the mobile phase in HPLC. The column temperature was 30°C, the flow rate was 0.15 ml min $^{-1}$ and the detection wavelength was 254 nm. For the analysis of Ph₃P and Ph₃PO, acetonitrile (80%) and water (20%) were used as the mobile phase. The flow rate was 0.2 ml min $^{-1}$ and the detection wavelength was 254 nm. For the analysis of reaction mixtures of the oxidation of *trans*-stilbene, acetonitrile (70%) and water (30%) were used as the mobile phase. The flow rate was 0.2 ml min $^{-1}$ and the detection wavelength was 226 nm.

The gas chromatography (GC) analysis was performed on an Agilent GC7890B system (FID detector) with a DB-VRX column ($20\,\mathrm{m} \times 180\,\mathrm{\mu m} \times 1\,\mathrm{\mu m}$). For the analysis of the product (cyclohexene oxide) after the oxidation of cyclohexene, the following GC conditions were used: $50\,^\circ\mathrm{C}$ (4 min), $10\,^\circ\mathrm{C}$ min⁻¹, $90\,^\circ\mathrm{C}$ (0 min), $10\,^\circ\mathrm{C}$ min⁻¹ and $185\,^\circ\mathrm{C}$ (0 min) on a DB-VRX column. The injection and detector temperatures were 200 and 230 °C, respectively. For the analysis of the reaction mixtures of the oxidation of cyclooctene, the following GC conditions were used: $50\,^\circ\mathrm{C}$ (2 min), $10\,^\circ\mathrm{C}$ min⁻¹ and $185\,^\circ\mathrm{C}$ (0 min) on a DB-VRX column. Injection and detector temperatures were 200 and 230 °C, respectively.

The isotope compositions of the products (MPSO and cyclooctene oxide) in the $\rm H_2^{18}O$ (97% atom ^{18}O) isotopic labelling experiments during the oxidation of MPS and cyclooctene were detected on an Agilent GC(7890B)-MS(5977 A) system. The GC conditions for cyclooctene oxide were as follow: 50°C (5 min), 5°C min $^{-1}$, 100°C (5 min), 20°C min $^{-1}$ and 200°C (0 min) on a HP-5MS column (30 m×250 µm×0.25 µm). Injection and detector temperatures were 150 and 220°C, respectively. The following GC conditions for MPSO were used: 50°C (3 min), 5°C min $^{-1}$, 140°C (2 min), 10°C min $^{-1}$ and 180°C (2 min) on a HP-5MS column. Injection and detector temperatures were 180 and 300°C, respectively.

The inorganic substrates (nitrite and phosphite) and their oxidized products were measured using an ion chromatograph (IC, Dionex ICS-900) equipped with an IonPac AS19 column (4×250 mm, Dionex), an eluent generator cartridge (Dionex EGC III KOH) and a conductivity detector. The eluent was 15 mM KOH solution, the flow rate was 1 ml min $^{-1}$ and the suppress current was 50 mA.

The arsenite substrate and its products were characterized by measuring $\mathrm{As^{V}}$ using the modified molybdate-based method*!. Briefly, 1 ml of the reaction solution was mixed with 0.3 ml of 2% HCl, 1 ml of methanol (for quenching the residual radicals) and 0.3 ml of molybdate reagent in a 4 ml cuvette. The absorbance was measured at 880 nm with a ultraviolet–visible spectrophotometer after 15 min. The arsenite substrate was measured after $\mathrm{As^{II}}$ was oxidized to $\mathrm{As^{V}}$ by a peroxymonosulfate anion.

NATURE CATALYSIS ARTICLES

All the concentrations of the substrates and products were determined by the integrated peak areas and calculated by standard curves, which were obtained from the authentic samples with given concentrations.

Computational details. DFT calculations were found to be in excellent agreement with experimental results with respect to predicting various properties for α-Fe₂O₃, which included lattice parameters, bandgap values and reaction energies. Spin-polarized DFT+U⁴⁹ calculations were performed with the Vienna Ab-initio Simulation Package^{50–53} at the generalized gradient approximation level with the Perdew-Burke-Ernzerhof exchange-correlation functional⁵⁴. Ion-electron interaction was described by the projector augmented wave method^{55,56}. An energy cutoff of 400 eV was adopted for the plane-wave basis set. The Gaussian smearing method was used and the σ value was chosen to be 0.2 eV unless otherwise noted. As Fe and Ti atoms contain strongly correlated 3d electrons, a U-J value (representing the spherically averaged intra-atomic Coulomb minus exchange energy of the localized d electrons that suffer the most from self-interaction error) of 4.3 eV that was derived ab initio was used for Fe atoms⁵⁷, and a typical U-I value of 4.0 eV was selected for Ti atoms⁵⁸. To better describe the dispersion interaction within systems, Grimme's D3 correction with the Becke-Johnson damping was adopted59,60

The slab model of α -Fe₂O₃(110) and rutile TiO₂(110) surfaces were constructed from their optimized bulk structures. According to the study by Durrant et al., the slab of hydroxyl terminated α -Fe₂O₃(110) contained four layers of Fe atoms, six layers of O atoms and hydroxyl groups on both sides of the slab44. A supercell of 8.81 Å × 13.91 Å × 26.17 Å, which contained a slab of 174 atoms and a vacuum layer of 15 Å, was used. The slab model of hydroxyl-terminated rutile TiO₂(110) was constructed by a supercell of 9.00 Å × 13.15 Å × 28.87 Å, which contained a slab of 180 atoms and a vacuum layer of 15 Å. For the slab calculation, only the Gamma point was included for the sampling of the Brillouin zone when the geometric structures were optimized, and a 3×3×1 Gamma-centred Monkhorst-Pack k-point sampling was chosen for the single-point calculations to obtain the refined electronic energies and DOS. For calculations of $H_2(g)$, the σ value was chosen to be 0.001 eV, and only the Gamma point was included for the sampling of the Brillouin zone. Structures were optimized until the maximum force on the atoms was smaller than 0.03 eV Å-1, and the energy convergence criterion was set to be 10⁻⁶ eV for all the structure relaxations unless otherwise noted.

Frequencies were calculated by diagonalizing a numerical Hessian matrix calculated with finite differences and a step size of 0.015 Å. In α -Fe₂O₃, only two Fe atoms, two terminal OH groups and one bridge OH group coordinated to the two Fe atoms were included. In TiO₂, only two Ti atoms, two terminal OH groups and two bridge O atoms coordinated to the two Ti atoms were included to calculate the numerical Hessian matrix. Vaspkit⁶⁴ was used to calculate thermal corrections to the Gibbs free energies. For reaction steps that involved H⁺ and e⁻, the computational hydrogen electrode model developed by Nørskov et al. $^{65.66}$ was used to calculate the free energy changes. The Gibbs free energy analysis was performed under standard conditions (pH=0, 298.15 K, 1 atm) and U=0.

The first hole trapping on $\alpha\text{-Fe}_2O_3$ is described by reaction (4). When the second hole accumulations on $\alpha\text{-Fe}_2O_3$ were modelled, two electronic configurations were considered: the formation of the two adjacent FeIV=O (reaction (5)) and the isolated FeV=O (reaction (6)). As the spin of the adjacent Fe atom is antiferromagnetically coupled in $\alpha\text{-Fe}_2O_3$, removal of two electrons from two adjacent Fe atoms, with the formation of the two adjacent FeIV=O bonds, would not change the difference between the number of electrons of spin up and spin down, and leads to a singlet for the spin multiplicity. If the two electrons are removed from one Fe atom for the formation of the isolated FeV=O, the spin multiplicity should be a triplet. To calculate the energy of FeIV-FeIV and FeV-FeIII, the same initial geometric structure was used and optimized. Triplet and singlet spin multiplicity was used to mimic the isolated FeV=O and two adjacent FeIV=O, respectively.

The first hole accumulation on TiO₂ is described by reaction (7).

$$Fe^{III} - Fe^{III} \rightarrow Fe^{IV} - Fe^{III} + H^+ + e^-$$
 (4)

$$Fe^{IV}-Fe^{III}\rightarrow Fe^{IV}-Fe^{IV}+H^++e^- \eqno(5)$$

$$Fe^{IV} - Fe^{III} \rightarrow Fe^{V} - Fe^{III} + H^{+} + e^{-}$$
 (6)

$$Ti^{IV}-OH\rightarrow Ti^{IV}-O+H^{+}+e^{-} \tag{7} \label{eq:7}$$

Data availability

The data that support the findings of this study, which include photoanode preparation, experimental procedures, material characterization, product analysis and computational details are available in the accompanying Supplementary Information or from the authors upon reasonable request. Source data are provided with this paper.

Received: 16 November 2019; Accepted: 28 June 2021; Published online: 09 August 2021

References

- 1. Grätzel, M. Photoelectrochemical cells. Nature 414, 338-344 (2001).
- Walter, M. G. et al. Solar water splitting cells. Chem. Rev. 110, 6446–6473 (2010).
- Wang, S., Liu, G. & Wang, L. Crystal facet engineering of photoelectrodes for photoelectrochemical water splitting. Chem. Rev. 119, 5192–5247 (2019).
- Zeng, Q. et al. Synthesis of WO₃/BiVO₄ photoanode using a reaction of bismuth nitrate with peroxovanadate on WO₃ film for efficient photoelectrocatalytic water splitting and organic pollutant degradation. Appl. Catal. B 217, 21–29 (2017).
- Li, T. et al. Photoelectrochemical oxidation of organic substrates in organic media. Nat. Commun. 8, 390 (2017).
- Tateno, H., Iguchi, S., Miseki, Y. & Sayama, K. Photo-electrochemical C–H bond activation of cyclohexane using a WO₃ photoanode and visible light. *Angew. Chem. Int. Ed.* 57, 11238–11241 (2018).
- Xiong, P. & Xu, H.-C. Chemistry with electrochemically generated N-centered radicals. Acc. Chem. Res. 52, 3339–3350 (2019).
- Yuan, Y. & Lei, A. Electrochemical oxidative cross-coupling with hydrogen evolution reactions. Acc. Chem. Res. 52, 3309–3324 (2019).
- Lum, Y. et al. Tuning OH binding energy enables selective electrochemical oxidation of ethylene to ethylene glycol. Nat. Catal. 3, 14–22 (2020).
- Zhang, P., Wang, Y., Li, H. & Antonietti, M. Metal-free oxidation of sulfides by carbon nitride with visible light illumination at room temperature. *Green Chem.* 14, 1904–1908 (2012).
- 11. Zhang, B. et al. Selective oxidation of sulfides on Pt/BiVO₄ photocatalyst under visible light irradiation using water as the oxygen source and dioxygen as the electron acceptor. *J. Catal.* 332, 95–100 (2015).
- Zandi, O. & Hamann, T. W. Determination of photoelectrochemical water oxidation intermediates on haematite electrode surfaces using operando infrared spectroscopy. *Nat. Chem.* 8, 778–783 (2016).
- 13. Zhang, Y. et al. Rate-limiting O-O bond formation pathways for water oxidation on hematite photoanode. J. Am. Chem. Soc. 140, 3264-3269 (2018).
- Cha, H. G. & Choi, K. S. Combined biomass valorization and hydrogen production in a photoelectrochemical cell. Nat. Chem. 7, 328–333 (2015).
- Lhermitte, C. R. & Sivula, K. Alternative oxidation reactions for solar-driven fuel production. ACS Catal. 9, 2007–2017 (2019).
- 16. Zhang, L. et al. Photoelectrocatalytic arene C-H amination. *Nat. Catal.* 2,
- 17. Cummings, C. Y., Marken, F., Peter, L. M., Wijayantha, K. G. & Tahir, A. A. New insights into water splitting at mesoporous α-Fe₂O₃ films: a study by modulated transmittance and impedance spectroscopies. *J. Am. Chem. Soc.* 134, 1228–1234 (2012).
- Chen, L. X., Liu, T., Thurnauer, M. C., Csencsits, R. & Rajh, T. Fe₂O₃ nanoparticle structures investigated by X-ray absorption near-edge structure, surface modifications, and model calculations. *J. Phys. Chem. B* 106, 8539–8546 (2002).
- Kronawitter, C. X. et al. Electron enrichment in 3d transition metal oxide hetero-nanostructures. Nano Lett. 11, 3855–3861 (2011).
- Braun, A. et al. Direct observation of two electron holes in a hematite photoanode during photoelectrochemical water splitting. *J. Phys. Chem. C* 116, 16870–16875 (2012).
- Kumar, A., Goldberg, I., Botoshansky, M., Buchman, Y. & Gross, Z. Oxygen atom transfer reactions from isolated (oxo)manganese(V) corroles to sulfides. J. Am. Chem. Soc. 132, 15233–15245 (2010).
- 22. Lionetti, D. et al. Effects of Lewis acidic metal ions (M) on oxygen-atom transfer reactivity of heterometallic Mn_3MO_4 cubane and $Fe_3MO(OH)$ and $Mn_3MO(OH)$ clusters. *Inorg. Chem.* **58**, 2336–2345 (2019).
- Paudel, J., Pokhrel, A., Kirk, M. L. & Li, F. Remote charge effects on the oxygen-atom-transfer reactivity and their relationship to molybdenum enzymes. *Inorg. Chem.* 58, 2054–2068 (2019).
- Li, Y. et al. Selective late-stage oxygenation of sulfides with ground-state oxygen by uranyl photocatalysis. *Angew. Chem. Int. Ed.* 58, 13499–13506 (2019).
- Jin, K. et al. Epoxidation of cyclooctene using water as the oxygen atom source at manganese oxide electrocatalysts. J. Am. Chem. Soc. 141, 6413–6418 (2019)
- Peariso, K., McNaughton, R. L. & Kirk, M. L. Active-site stereochemical control of oxygen atom transfer reactivity in sulfite oxidase. *J. Am. Chem. Soc.* 124, 9006–9007 (2002).

- McGarrigle, E. M. & Gilheany, D. G. Chromium

 and manganese–salen promoted epoxidation of alkenes. Chem. Rev. 105, 1563–1602 (2005).
- Avenier, F. et al. Photoassisted generation of a dinuclear iron(III) peroxo species and oxygen-atom transfer. *Angew. Chem. Int. Ed.* 52, 3634–3637 (2013).
- Kang, Y. et al. Mutable properties of nonheme iron(III)-iodosylarene complexes result in the elusive multiple-oxidant mechanism. J. Am. Chem. Soc. 139, 7444–7447 (2017).
- Serrano-Plana, J. et al. Exceedingly fast oxygen atom transfer to olefins via a catalytically competent nonheme iron species. *Angew. Chem. Int. Ed.* 55, 6310–6314 (2016).
- Ling, Y., Wang, G., Wheeler, D. A., Zhang, J. Z. & Li, Y. Sn-doped hematite nanostructures for photoelectrochemical water splitting. *Nano Lett.* 11, 2119–2125 (2011).
- Goto, Y., Matsui, T., Ozaki, S.-I., Watanabe, Y. & Fukuzumi, S. Mechanisms of sulfoxidation catalyzed by high-valent intermediates of heme enzymes: electron-transfer vs oxygen-transfer mechanism. *J. Am. Chem. Soc.* 121, 9497–9502 (1999).
- 33. Li, Y., Wang, M. & Jiang, X. Controllable sulfoxidation and sulfenylation with organic thiosulfate salts via dual electron- and energy-transfer photocatalysis. *ACS Catal.* 7, 7587–7592 (2017).
- Chen, X. & Mao, S. S. Titanium dioxide nanomaterials: synthesis, properties, modifications, and applications. *Chem. Rev.* 107, 2891–2959 (2007).
- Nosaka, Y. & Nosaka, A. Y. Generation and detection of reactive oxygen species in photocatalysis. Chem. Rev. 117, 11302–11336 (2017).
- Hansch, C., Leo, A. & Taft, R. W. A survey of Hammett substituent constants and resonance and field parameters. Chem. Rev. 91, 165–195 (1991).
- Badalyan, A. & Stahl, S. S. Cooperative electrocatalytic alcohol oxidation with electron-proton-transfer mediators. *Nature* 535, 406–410 (2016).
- 38. Engelmann, X. et al. Trapping of a highly reactive oxoiron(IV) complex in the catalytic epoxidation of olefins by hydrogen peroxide. *Angew. Chem. Int. Ed.* **58**, 4012–4016 (2019).
- Lee, Y. M. et al. Direct oxygen atom transfer versus electron transfer mechanisms in the phosphine oxidation by nonheme Mn(IV)–oxo complexes. *Chem. Commun.* 53, 9352–9355 (2017).
- Man, W.-L., Lam, W. W. Y., Wong, W.-Y. & Lau, T.-C. Oxidation of nitrite by a trans-dioxoruthenium(VI) complex: direct evidence for reversible oxygen atom transfer. J. Am. Chem. Soc. 128, 14669–14675 (2006).
- Wang, Z., Bush, R. T., Sullivan, L. A., Chen, C. & Liu, J. Selective oxidation of arsenite by peroxymonosulfate with high utilization efficiency of oxidant. *Environ. Sci. Technol.* 48, 3978–3985 (2014).
- Klahr, B., Gimenez, S., Fabregat-Santiago, F., Hamann, T. & Bisquert, J. Water oxidation at hematite photoelectrodes: the role of surface states. *J. Am. Chem.* Soc. 134, 4294–4302 (2012).
- 43. Le Formal, F. et al. Rate law analysis of water oxidation on a hematite surface. J. Am. Chem. Soc. 137, 6629–6637 (2015).
- Mesa, C. A. et al. Multihole water oxidation catalysis on haematite photoanodes revealed by operando spectroelectrochemistry and DFT. Nat. Chem. 12, 82–89 (2020).
- Yatom, N., Neufeld, O. & Caspary Toroker, M. Toward settling the debate on the role of Fe₂O₃ surface states for water splitting. *J. Phys. Chem. C* 119, 24789–24795 (2015).
- Kundu, S., Thompson, J. V., Ryabov, A. D. & Collins, T. J. On the reactivity of mononuclear iron(V)oxo complexes. J. Am. Chem. Soc. 133, 18546–18549 (2011).
- Singh, K. K., Tiwari, M. K., Dhar, B. B., Vanka, K. & Gupta, S. S. Mechanism of oxygen atom transfer from Fe^v(O) to olefins at room temperature. *Inorg. Chem.* 54, 6112–6121 (2015).
- Lim, M. H. et al. An Fe^{IV}=O complex of a tetradentate tripodal nonheme ligand. Proc. Natl Acad. Sci. USA 100, 3665–3670 (2003).
- Dudarev, S. L., Botton, G. A., Savrasov, S. Y., Humphreys, C. J. & Sutton, A. P. Electron-energy-loss spectra and the structural stability of nickel oxide: an LSDA+U study. *Phys. Rev. B* 57, 1505–1509 (1998).
- Kresse, G. & Hafner, J. Ab initio molecular dynamics for liquid metals. Phys. Rev. B 47, 558–561 (1993).
- Kresse, G. & Hafner, J. Ab initio molecular-dynamics simulation of the liquid-metal-amorphous-semiconductor transition in germanium. *Phys. Rev. B* 49, 14251–14269 (1994).

- Kresse, G. & Furthmuller, J. Efficiency of ab-initio total energy calculations for metals and semiconductors using a plane-wave basis set. *Comp. Mater.* Sci. 6, 15–50 (1996).
- Kresse, G. & Furthmuller, J. Efficient iterative schemes for ab initio total-energy calculations using a plane-wave basis set. *Phys. Rev. B* 54, 11169–11186 (1996).
- 54. Perdew, J. P., Burke, K. & Ernzerhof, M. Generalized gradient approximation made simple. *Phys. Rev. Lett.* 77, 3865–3868 (1996).
- Blochl, P. E. Projector augmented-wave method. *Phys. Rev. B* 50, 17953–17979 (1994).
- Kresse, G. & Joubert, D. From ultrasoft pseudopotentials to the projector augmented-wave method. *Phys. Rev. B* 59, 1758–1775 (1999).
- Mosey, N. J., Liao, P. & Carter, E. A. Rotationally invariant ab initio evaluation of Coulomb and exchange parameters for DFT+U calculations. J. Chem. Phys. 129, 014103 (2008).
- 58. Ji, Y., Fan, T. & Luo, Y. First-principles study on the mechanism of photocatalytic reduction of nitrobenzene on the rutile TiO₂(110) surface. *Phys. Chem. Chem. Phys.* 22, 1187–1193 (2019).
- Grimme, S., Antony, J., Ehrlich, S. & Krieg, H. A consistent and accurate ab initio parametrization of density functional dispersion correction (DFT-D) for the 94 elements H–Pu. *J. Chem. Phys.* 132, 154104 (2010).
- Grimme, S., Ehrlich, S. & Goerigk, L. Effect of the damping function in dispersion corrected density functional theory. *J. Comput. Chem.* 32, 1456–1465 (2011).
- Monkhorst, H. J. & Pack, J. D. Special points for Brillouin-zone integrations. Phys. Rev. B 13, 5188–5192 (1976).
- 62. Finger, L. W. & Hazen, R. M. Crystal structure and isothermal compression of Fe_2O_3 , Cr_2O_3 , and V_2O_3 to 50 kbars. *J. Appl. Phys.* **51**, 5362–5367 (1980).
- Hanaor, D. A. H. & Sorrell, C. C. Review of the anatase to rutile phase transformation. J. Mater. Sci. 46, 855–874 (2011).
- Wang, V., Xu, N., Liu, J.-C., Tang, G. & Geng, W.-T. VASPKIT: a pre- and post-processing program for VASP code. *Cond. Mat. Mater. Sci.* 267, 108033 (2021).
- Nørskov, J. K. et al. Origin of the overpotential for oxygen reduction at a fuel-cell cathode. J. Phys. Chem. B 108, 17886–17892 (2004).
- Nørskov, J. K. et al. Trends in the exchange current for hydrogen evolution. J. Electrochem. Soc. 152, J23–J26 (2005).

Acknowledgements

This work was supported by the Strategic Priority Research Program of the Chinese Academy of Sciences, grant no. XDB36000000, NSFC (nos. 21777168, 21827809 and 22072158) and the 'National Key R&D Program of China' (nos. 2018YFA0209302 and 2020YFC1808401).

Author contributions

Y. Zhao and C.C. conceived and designed the experiments. Y. Zhao performed most of the experiments. C.D. prepared $\alpha\text{-Fe}_2O_3$ and contributed the DFT work. D.T. reproduced the results of MPS photoelectrolysis experimental data. L.D. measured and analysed the scanning electron microscopy data. Y. Zhao, C.D., D.T., L.D., Y. Zhang, H.S., H.J., W.S., W.M., C.C. and J.Z. analysed the results and reviewed the paper. C.C., Y. Zhao. and Y. Zhang wrote the paper, with input from the other authors. C.C. directed the project.

Competing interests

The authors declare no competing interests.

Additional information

Supplementary information The online version contains supplementary material available at https://doi.org/10.1038/s41929-021-00659-1.

Correspondence and requests for materials should be addressed to Y.Z., C.C. or J.Z.

Peer review information *Nature Catalysis* thanks Victor Batista, Alberto Vomiero, Li-Zhu Wu and the other, anonymous, reviewer(s) for their contribution to the peer review of this work.

Reprints and permissions information is available at www.nature.com/reprints.

Publisher's note Springer Nature remains neutral with regard to jurisdictional claims in published maps and institutional affiliations.

© The Author(s), under exclusive licence to Springer Nature Limited 2021